J. Fluid Mech. (1985), *vol.* 158, *pp.* 269–287
Printed in Great Britain

Waves due to a steadily moving source on a floating ice plate

By J. W. DAVYS, R. J. HOSKING AND A. D. SNEYD
University of Waikato, Hamilton, New Zealand.

(Received 15 November 1984 and in revised form 14 March 1985)

The propagation of flexural waves in floating ice plates is governed by two restoring forces – elastic bending of the plate, and the tendency of gravity to make the upper surface of the supporting water horizontal. This paper studies steady wave patterns generated by a steadily moving source on a water–ice system that is assumed to be homogeneous and of infinite horizontal extent, using asymptotic Fourier analysis to give a simple description of the wave pattern far from the source. Short-wavelength elastic waves propagate ahead, while the long gravity waves appear behind; and, depending on the system parameters, one, two or no caustics may appear. Wavecrest patterns are shown, and the amplitude variation with direction from the source is given. Where the two caustics just merge together, a special mathematical function analogous to the Airy function is introduced to describe wave amplitudes. These waves can be detected by a strainmeter embedded in the ice, and we compare its theoretical response with some experimental measurements.

1. Introduction

The sea-ice cover in McMurdo Sound, Antarctica, has been used as an aircraft runway since the International Geophysical Year (1957/58). When the ice is about $2\frac{1}{2}$ m thick it can support large aircraft such as the LC-130 Hercules carrying heavy payloads, but since it changes seasonally there is a restricted period of safe operation – usually mid-August to mid-December. Predicting ice strength is thus a matter of some practical importance.

As an aircraft comes in to land, the ground immediately beneath is subject to increased air pressure, the total excess pressure force equalling the aircraft weight. This travelling force generates a system of waves which propagate through the ice and the water it floats on, in much the same way as a ship sets up the well-known Kelvin wave pattern. Instruments placed on the ice can detect these waves, and analysis of the data could provide information on the ice sheet, without the aircraft even touching down. At McMurdo Sound these waves were first recorded on a strainmeter built and maintained by members of the Physics Department of the University of Waikato (Funnell 1982).

For analytical purposes a reasonable model is an elastic homogeneous ice plate of infinite extent, resting on incompressible inviscid fluid of constant depth. (Over long timescales ice can behave as a viscoelastic material, but this effect is ignored here.) The dispersion relation for plane waves in this system was given almost 100 years ago by Greenhill (1887). Kerr (1976) gives a comprehensive survey of research into the response of floating ice to static loads, and Kheisin (1971) studies the effect of a concentrated line load that begins to move at time $t = 0$. A steady load moving with constant speed V is considered by Nevel (1970), but as with most previous work

the emphasis is on calculating stresses near the load region, with a view to predicting fracture. Here we are more concerned with determining the wave field far from the aircraft where the recording instrument would be placed. Since we shall also assume that the waves are generated by a constant load travelling at constant speed, a suitable mathematical technique is asymptotic Fourier analysis – c.f. for example Lighthill (1978). This technique has been applied by Mills (1972) to steadily moving oscillatory loads, but this paper is rather inaccessible and gives only a sketchy picture of the wavecrest pattern with little discussion of cusps and caustics. It also contains an important mistake.

The dispersion relation for waves in the model system is discussed in §2. Since there are two restoring forces – elastic forces from the bending of the ice plate, and gravity forces as for ordinary water waves – there are two limiting wave types. Short-wavelength elastic waves have a group velocity greater than their phase velocity and propagate ahead of the source, whereas the longer gravity waves propagate behind. In §3 the wavecrest pattern is described, which varies dramatically with source speed V and to a lesser extent with other parameters. Of particular interest are caustics, and, depending on the value of V, one, two or no caustics may be present. For large enough V a shadow zone without waves forms behind the source. Section 4 describes the variation in wave amplitude (and hence energy) with direction from the source, and it appears that most energy is radiated by the gravity-wave part of the spectrum, particularly near the caustics. Where two caustics just merge, a special mathematical function analogous to the Airy function is necessary, which is discussed in the Appendix. Section 5 describes the geophysical wire strainmeter that has been used to detect the presence of waves, and we calculate its theoretical response as a function of time during an aircraft approach. Comparison is then made with experimental measurements.

2. Dispersion relation

Consider an infinite homogeneous ice sheet of thickness h and density ρ_i floating on water of density ρ, as shown in figure 1. The upper undisturbed water surface is $z = 0$ and the equation of the sea bed $z = -H$. If $\eta(x, y, t)$ represents a small vertical ice-sheet deflection, then the equation of motion of the ice sheet is

$$D\nabla^4\eta + \rho_i h\eta_{tt} = p - f(x, y, t), \tag{2.1}$$

where

$$D = \frac{Eh^3}{12(1-\nu^2)},$$

E being Young's modulus and ν Poisson's ratio for ice, p the water pressure at $z = 0$ and $f(x, y, t)$ the downward external stress exerted on the ice. The sea water flow is taken to be irrotational with velocity potential ϕ, so that Bernoulli's theorem gives

$$p = -\rho(\phi_t)_{z=0} - \rho g\eta. \tag{2.2}$$

Combining (2.1) and (2.2), we find

$$D\nabla^4\eta + \rho_i h\eta_{tt} = -\rho(\phi_t)_{z=0} - \rho g\eta - f. \tag{2.3}$$

In (2.2) and (2.3) we have made the usual linear wave-theory approximation of evaluating perturbed quantities on $z = 0$ rather than the true water surface $z = \eta$. Typical figures for ice in McMurdo Sound would be $E = 5 \times 10^9$ N m^{-2}, $h = 2.5$ m, $H = 350$ m and $\nu = \frac{1}{3}$. Unless otherwise stated, all calculations will be based on these parameter values. A typical source speed (aircraft landing speed) is $V = 50$ m/s.

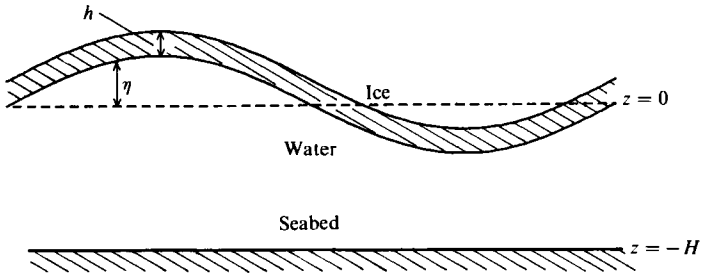

FIGURE 1. Diagram of floating ice plate.

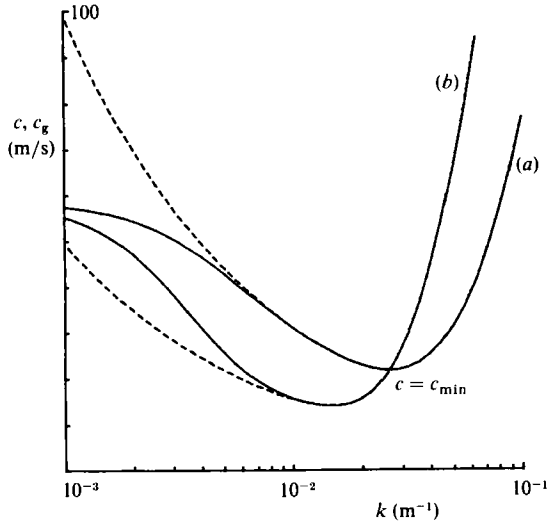

FIGURE 2. Graphs of phase speed (a) and group speed (b) against wavenumber k. The solid curves are for water of depth 350 m and the dashed curves for water of infinite depth. Note that the wavenumber scale is logarithmic.

The dispersion relation for uniform plane waves with η everywhere proportional to $\exp[\mathrm{i}(kx-\omega t)]$ can be found by substitution into (2.3) with $f = 0$, and using the kinematic boundary condition

$$\eta_t = (\phi_z)_{z=0} = k \tanh kH \, (\phi)_{z=0}.$$

One obtains

$$\omega^2 = \frac{Dk^5/\rho + gk}{kh' + \coth kH}, \quad h' = \frac{\rho_i h}{\rho}. \tag{2.4}$$

Figure 2 shows graphs of the phase speed $c = \omega/k$ and group speed $c_g = \mathrm{d}\omega/\mathrm{d}k$ against k for the McMurdo Sound parameters, and also for infinitely deep water.

There are three important lengthscales associated with this dispersion relation – a short scale characterized by the (modified) ice thickness h', a long scale characterised by the water depth H, and an intermediate scale corresponding to the reciprocal wavenumber $k_I^{-1} \approx (3D/\rho g)^{\frac{1}{4}} \approx 40$ m for which the phase speed is minimum, and where the effects of ice elasticity and gravity are comparable. For very short waves where $kh' \geqslant O(1)$

$$\omega^2 \approx \frac{D}{h'\rho} k^4$$

and the group speed is twice the phase speed, so these elastic-dominated waves appear ahead of the moving source. Since $k_I h' \ll 1$ and $k_I H \gg 1$, the dispersion relation for waves of intermediate length can be approximated by

$$\omega^2 \approx \frac{Dk^5}{\rho} + gk;$$

and the minimum phase speed $c_{\min}$, at which the group and phase speeds are equal, is therefore given by

$$c_{\min} \approx 2\left(\frac{Dg^3}{27\rho}\right)^{\frac{1}{8}} = 22.5 \text{ m/s}. \tag{2.5}$$

For long waves where $kH \leqslant O(1)$

$$\omega^2 \approx gk \tanh kH,$$

which is just the dispersion relation for gravity waves on water of depth H. Their group speed is less than their phase speed, so they appear behind the source.

For all but the very shortest waves ($kh' \geqslant O(1)$) the dispersion relation (2.4) can be approximated by

$$\omega^2 = \left(\frac{Dk^4}{\rho g} + 1\right) gk \tanh kH. \tag{2.6}$$

We shall be concerned only with waves longer than about 50 m, so we can use (2.6) instead of (2.4) without significant loss of accuracy – i.e. we may ignore the small ice-sheet acceleration term in (2.1).

3. Steady wave patterns

Asymptotic Fourier analysis

Equation (2.3) may be solved formally by taking a Fourier transform in x, y and t:

$$\hat{\eta}(l, m, \omega) = (2\pi)^{-\frac{3}{2}} \int \eta(x, y, t)\, e^{i(lx+my-\omega t)}\, dx\, dy\, dt.$$

Assuming that the disturbance tends to zero at infinity, one finds

$$\hat{\eta} = \frac{-\hat{f}(l, m, \omega)}{Dk^4 + \rho g - \rho h' \omega^2 - (\rho\omega^2/k) \coth kH}, \tag{3.1}$$

where $k^2 = l^2 + m^2$. If we now suppose that $f(x, y, t)$ represents a steady stress distribution travelling with speed V in the x-direction, we can write

$$f(x, y, t) = F(x - Vt, y),$$

so that

$$\hat{f}(l, m, \omega) = (2\pi)^{\frac{1}{2}} \delta(Vl - \omega)\, \hat{F}(l, m), \tag{3.2}$$

where the Fourier transform $\hat{F}$ is taken with respect to only two variables, and δ denotes the Dirac delta function.

For a steady wave pattern, the component of the source velocity $V\hat{\boldsymbol{x}}$ normal to any wave crest must equal the crest phase speed, i.e.

$$\frac{Vl}{k} = \omega/k \quad \text{or} \quad c = V \cos\beta, \tag{3.3a, b}$$

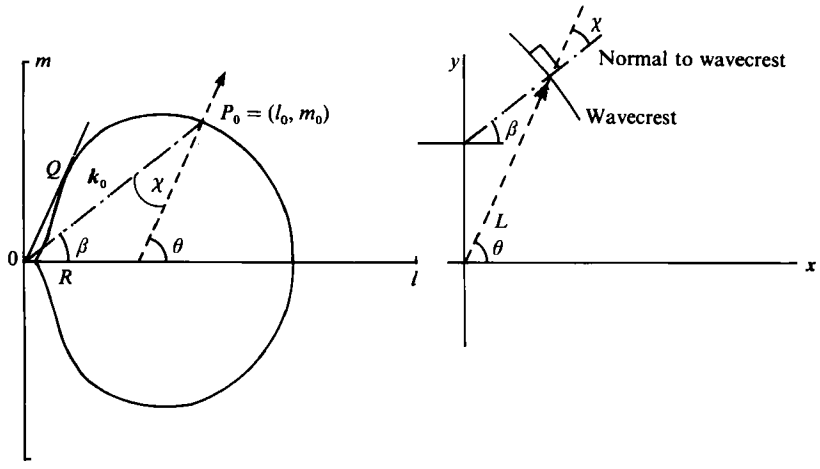

FIGURE 3. (*a*) Wavenumber curve C_k for $V = 50$ m/s. (*b*) Wavecrest construction in (x, y)-plane.

where β is the angle between the wavenumber vector $\boldsymbol{k}$ and the source velocity (see figure 3). This condition is reflected by the presence of the delta function in (3.2). Fourier inversion of (3.1) gives

$$\eta = -\frac{1}{2\pi}\int\frac{\hat{F}(l, m)}{B(l, m)}\mathrm{e}^{-\mathrm{i}[l(x-Vt)+my]}\,\mathrm{d}l\,\mathrm{d}m, \tag{3.4}$$

where

$$B(l, m) = Dk^4 + \rho g - \rho h' V^2 l^2 - \frac{\rho V^2 l^2}{k}\coth kH. \tag{3.5}$$

Note that $B(l, m) = 0$ is just the dispersion relation (2.4) with ω replaced by Vl according to (3.3*a*).

Generally one would not expect to be able to evaluate the integral in (3.4) analytically, although several special cases for simple loading functions f are considered by Nevel (1970). To describe the wave pattern we need to know η far away from the region where load is applied, so we can use asymptotic methods – cf. for example Lighthill (1978, §4.9 *et seq*). The wave pattern is determined from the *wavenumber curve* C_k in the (l, m)-plane, whose equation $B(l, m) = 0$ is the steady-wave condition (3.3) combined with the dispersion relation (2.4). Only waves with wavenumbers lying on C_k will appear in the steady pattern. From any point $(l_0, m_0) = P_0$ say, on C_k, waves are radiated in the direction of the normal to C_k at that point (in the sense of increasing ω) along the line L in the corresponding direction in the (x, y)-plane, as shown in figure 3. The time of observation is always chosen to be the instant the travelling load reaches the origin of the (x, y)-plane, so that waves are always radiated from this point. The ice displacement η is given by the formula

$$\eta \approx -\hat{F}(l_0, m_0)\left[\left(\frac{\partial B}{\partial n}\right)_0\right]^{-1}\left(\frac{2\pi}{\kappa_0 r}\right)^{\frac{1}{2}}\mathrm{e}^{-\mathrm{i}(l_0 x + m_0 y + \Theta)}, \tag{3.6}$$

where r is distance from the origin (or source), κ_0 is the magnitude of the curvature of C_k at P_0, $\partial/\partial n$ is differentiation normal to C_k in the sense of ω increasing, and Θ is a phase factor $= \frac{1}{4}\pi$ if C_k is convex to the n-direction at P_0 and $\frac{3}{4}\pi$ otherwise. Sometimes there are several points on C_k at which the normal is parallel to a given

direction, in which case η is the sum of contributions of the form (3.6) from each such point.

The wave crests are lines of constant phase,

$$l_0 x + m_0 y = \boldsymbol{x} \cdot \boldsymbol{k}_0 = K$$

(see figure 3), where K is a constant. Thus to each point P_0 on C_k there corresponds a point on the wavecrest, whose polar coordinates in the (x, y)-plane are

$$\left(\frac{K}{k_0 \cos\chi}, \theta\right).$$

As P_0 moves around C_k, the above point will trace out a wavecrest. At any point of inflection on C_k the corresponding line L will be a caustic, and wavecrests will have cusps at their points of intersection with L.

In figure 3, Q is the point on C_k such that OQ is a tangent. Since β is maximum at Q it follows from (3.3b) that c is a minimum and that $c = c_{\min} = c_g$ at this point. As P_0 approaches Q from either side, $\chi \to \frac{1}{2}\pi$, so the wavecrest goes off to infinity. Thus wavecrests can be divided into two classes – those emanating from points on C_k to the left of Q where $c > c_g$, and which constitute the predominantly gravity-wave region, and the predominantly elastic waves from points to the right of Q where $c < c_g$.

Effect of source speed

Figure 4 shows wavenumber curves for different values of the source speed V, other parameters being held constant. For a typical V of 50 m/s each symmetric half of C_k has two points of inflection giving rise to two caustics, and as V decreases, these move together and eventually coincide when $V = V_s$, say, $= 37.5$ m/s. If V is further decreased, the points of inflection disappear. Points of inflection are not easily seen on C_k, and figure 5 shows graphs of the angle θ between the normal to C_k and the l-axis against k. The wavecrest patterns corresponding to three of the curves in figure 4 are shown in figure 6. For $V = 50$ m/s each crest in the gravity-wave region has two cusps, while for the smaller V-values there are none.

It can be seen from figure 2 that the maximum phase speed for gravity-dominated waves ($c > c_g$) is attained in the long wavelength limit and is equal to $(gH)^{\frac{1}{2}} = V_c$, say. Thus (3.3b) shows that for gravity waves

$$\frac{c_{\min}}{V} \leqslant \cos\beta \leqslant \frac{V_c}{V},$$

so if $V < V_c$, β ranges from 0 to $\cos^{-1}(c_{\min}/V)$, while if $V > V_c$ the lower bound for β is $\cos^{-1}(V_c/V)$. In the latter case β is always strictly greater than 0, so that no gravity waves appear directly behind the source. Such waves emanate from R, the leftmost point of intersection of C_k with the l-axis, so if $V > V_c$ the point R cannot exist – i.e. C_k must pass through the origin. (Mills (1972) presents graphs that incorrectly show C_k intersecting the m-axis away from the origin.)

Close to the origin the wavenumber curve can be approximated by

$$\frac{V^2}{V_c^2}\cos^2\beta = 1 - \tfrac{1}{3}k^2H^2, \tag{3.7}$$

where we have used the small-argument expansion $\tanh x \approx x - \frac{1}{3}x^3$. For $V < V_c$ (3.7) can be written in the form

$$k^2 = k_1^2 + \frac{3V^2}{H^2V_c^2}\sin^2\beta, \tag{3.8}$$

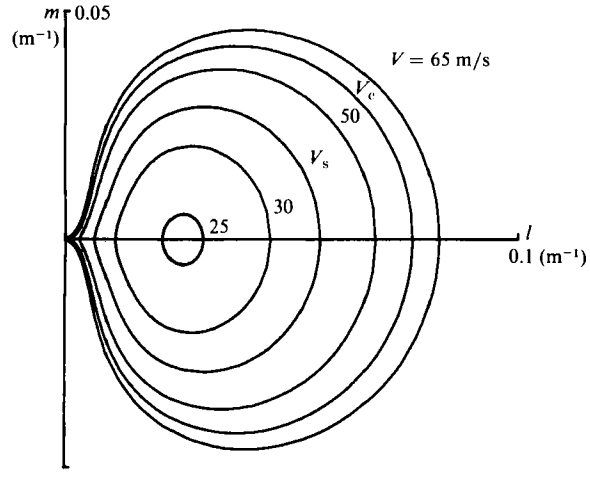

FIGURE 4. Wavenumber curves C_k for a variety of speeds. The curve $V = 50$ has two points of inflection. As V decreases, these move together and coincide when $V = V_s = 37.5$, so that this curve has a very straight section. For smaller values of V there are no points of inflection, and for values larger than V_c there is just one. Note that as V decreases towards $c_{min} = 22.5$ the curves shrink towards a single point.

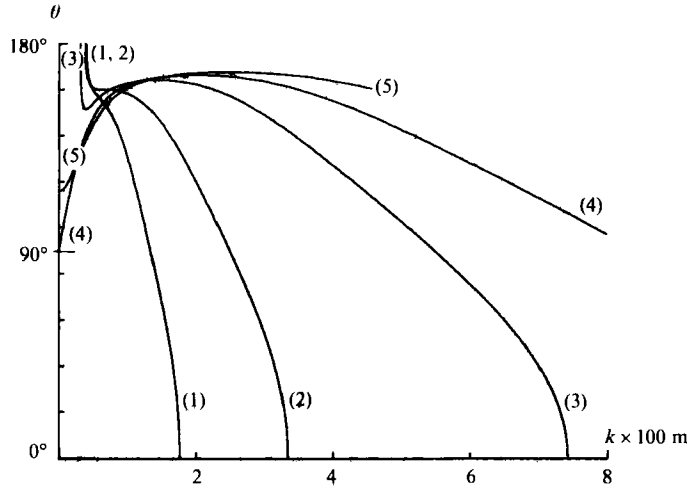

FIGURE 5. Graphs of the angle θ between the normal to C_k and the l-axis, against wavenumber k: (1) source velocity $V = 30.0$ m/s; (2) 37.5 m/s ($= V_s$); (3) 50.0 m/s; (4) 58.6 m/s ($= V_c$); (5) 65.0 m/s.

where (k, β) are polar coordinates in the (l, m)-plane, and $k_1 = [3(V_c^2 - V^2)]^{\frac{1}{2}}/HV_c$ is the coordinate of the intersection point R. If $V = V_c$ (3.7) becomes

$$k = \pm \frac{\sqrt{3}}{H} \sin\beta,$$

which represents a pair of circular arcs touching at the origin, and finally if $V > V_c$ the approximate form of (3.7) is

$$k^2 = \frac{3V^2}{H^2 V_c^2} (\cos^2\beta_0 - \cos^2\beta), \quad \beta_0 = \cos^{-1}\frac{V_c^2}{V^2},$$

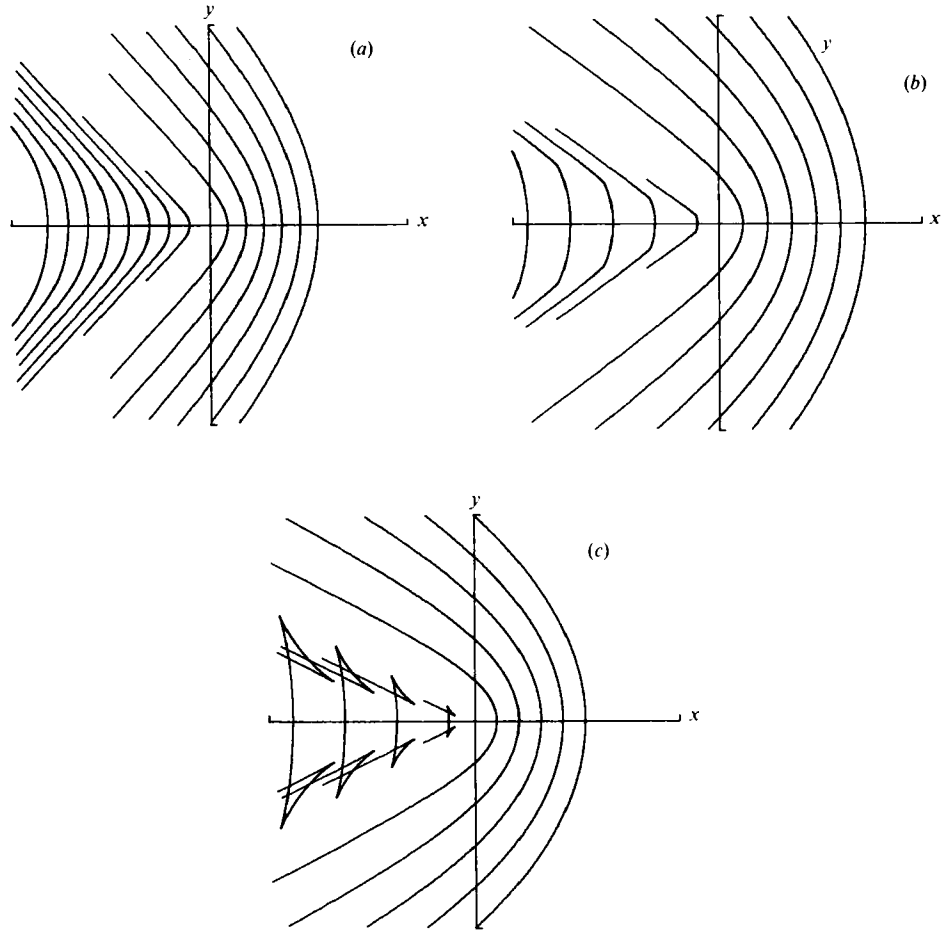

FIGURE 6. Wavecrest patterns for (a) $V = 30$ m/s, there are no caustics and no cusps; (b) 37.5 m/s, the two caustics have merged and there are no cusps; (c) 50 m/s, C_k has two points of inflection, so there are two caustics and wavecrests in this region have two cusps.

which represents a pair of curves intersecting at the origin and making angles $\pm\beta_0$ with the l-axis. Figure 7 shows the part of C_k close to the origin for various values of V close to V_c.

When $V < V_c$ and C_k does not pass through the origin, then the angle between its normal and the l-axis assumes all possible values from 0° to 360°, so that waves are radiated in all directions. But if $V \geqslant V_c$ this angle will not exceed a certain value θ_{max}, say, which is somewhat less than 180° (see figure 5). In the corresponding wave pattern (figure 8) a shadow zone appears behind the source, no waves being radiated into the triangular region $\theta_{max} \leqslant \theta \leqslant 360° - \theta_{max}$. Despite the sudden appearance of this shadow zone, η remains a continuous function of V as this variable increases through V_c. From figure 7 we can see that for V just less than V_c (curves 1 and 2), the portion of C_k that radiates waves almost directly behind the source – i.e. that portion close to the origin – has large curvature, so that the amplitude of η will be small. Indeed this amplitude tends to zero as $V \to V_c$ from below.

Figure 9 is a graph of the caustic directions against V, and shows the three regions where there are no caustics, two caustics or one caustic. If V is just less than V_c then the curve (3.8), which approximates C_k close to the origin, has a single point of

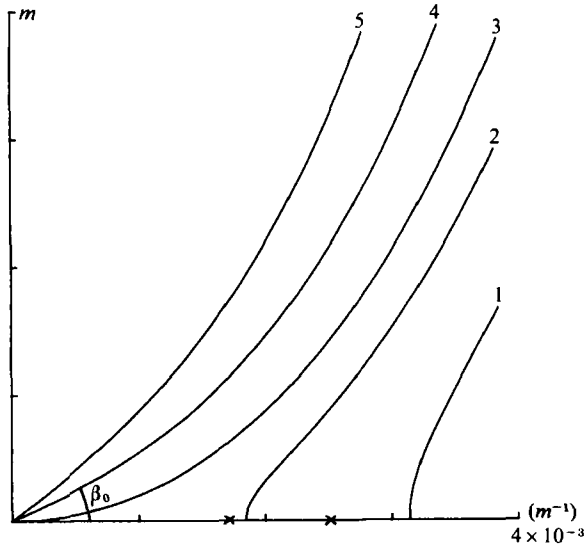

FIGURE 7. Wavenumber curve C_k near the origin for water of depth 350 m: (1) source velocity $V = 50.0$ m/s; (2) 55.0 m/s; (3) 58.6 m/s ($= V_c$); (4) 65.0 m/s; (5) 75.0 m/s. The crosses mark the approximate points of intersection $l = k_1$ (see (3.8)) of the curves with the l-axis, when $V < V_c$.

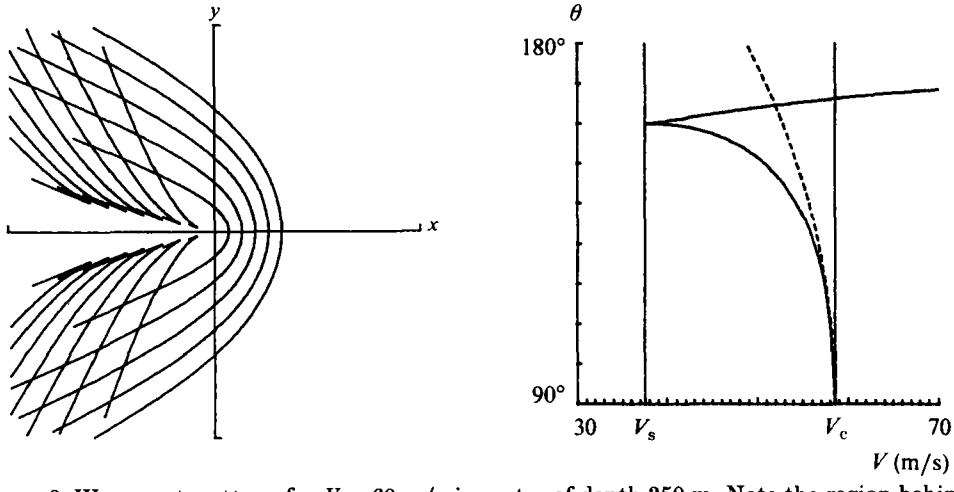

FIGURE 8. Wavecrest pattern for $V = 60$ m/s in water of depth 350 m. Note the region behind the source where no waves appear.

FIGURE 9. Graph of caustic directions against source speed V. The dashed curve represents the approximate formula (3.9).

inflection at $\beta \approx (\frac{1}{2}\epsilon)^{\frac{1}{2}}$, where $\epsilon = 1 - V^2/V_c^2$ is small. At this point the angle between the tangent and the positive l-axis $\approx 2(2\epsilon)^{\frac{1}{2}}$, so the first caustic direction is given by

$$\theta \approx \tfrac{1}{2}\pi + 2\left[2\left(1-\frac{V^2}{V_c^2}\right)\right]^{\frac{1}{2}}, \tag{3.9}$$

which reflects the behaviour of the lower curve in the two-caustic region of figure 9 as $V \to V_c$.

Figures 6(*c*) and 8 show regions of intersecting wavecrests. This situation arises when there is more than one point of C_k where the normal direction is equal to the

direction from the source, so that waves of different wavenumbers are radiated into the same region. In such a region the wave phase is undefined.

Critical speed

Figure 2 shows that the phase speed c has a minimum value $c_{\min}$ – often called the *critical speed* – where

$$c = c_{\min} = c_g \approx 22.5 \text{ m/s}.$$

Equation (3.3*b*) shows that β cannot exceed

$$\beta_{\max} = \cos^{-1}\frac{c_{\min}}{V}.$$

Figures 6(*a–c*) all correspond to $V > c_{\min}$, so that $\beta_{\max}$ is a well-defined angle between 0° and 90°. As V decreases towards $c_{\min}$, $\beta_{\max} \to 0$ and the wavecrests tend to become straight and perpendicular to V. Also the wavenumber curve C_k shrinks and degenerates to a single point when $V = c_{\min}$, so at this critical speed only waves of phase speed $c_{\min}$ propagating parallel to V appear in the steady pattern. When $V = c_{\min}$ we also have $V = c_g$, so for a source travelling at the critical speed energy is radiated directly forward at the same speed and will continuously accumulate underneath the source.† For $V = c_{\min}$ no steady wavepattern can exist (unless some energy-dissipation mechanism is included in the model), and the energy density close to the source will grow linearly in time. Since energy density is proportional to the square of the ice deflection, the latter will increase as $t^{\frac{1}{2}}$, as found by Kheisin (1971) for the corresponding two-dimensional problem.

It is well known that considerably amplified deflections can occur if a vehicle is driven over ice at a certain speed, which depends on ice thickness and water depth. Nevel (1970) found his expressions for ice deflection to be singular at a certain value of V, which can be identified mathematically with $c_{\min}$ (see Davys 1984, §2.4). Squire *et al.* (1985) have identified $c_{\min}$ as the vehicle speed that produces maximum compressive strain in the ice, and have used measurements of $c_{\min}$ to estimate E (cf. (2.5)).

If $V < c_{\min}$ a steady wavepattern cannot be established, since (3.3) cannot be satisfied. Any waves generated by the source will radiate away from it.

Water waves have properties that are quite similar to those we have just described – surface tension playing the role of ice-sheet elasticity. Longuet-Higgins (1977) has drawn closed wavenumber curves for gravity–capillary waves which are similar to the C_k shown in figure 4, and a discussion of related effects for water waves may be found for example in Lighthill (1978, §§3.9, 3.10).

4. Wave amplitudes

From (3.6) one sees that the wave amplitude falls off as $r^{-\frac{1}{2}}$ and is proportional to $\kappa_0^{-\frac{1}{2}}$. Thus relatively straight sections of C_k where κ_0 is small give rise to large wave amplitudes, because all points of that section radiate waves in approximately the same direction. At a point of inflection of C_k, $\kappa_0 = 0$ and (3.6) predicts an infinite amplitude. In this case the asymptotic expression must be modified, and for waves radiated from the neighbourhood of a point of inflection P_0 one finds

$$\eta = -\frac{2\pi i \hat{F}(l_0, m_0)}{(\partial B/\partial n)_0} e^{-i(l_0 x + m_0 y)} \left[\frac{2}{r\kappa_s}\right]^{\frac{1}{3}} \mathrm{Ai}\left[d\left(\frac{2}{r\kappa_s}\right)^{\frac{1}{3}}\right], \tag{4.1}$$

† We understand that M. J. Hinchey has independently made this identification of the critical speed with the group speed in a paper not yet published.

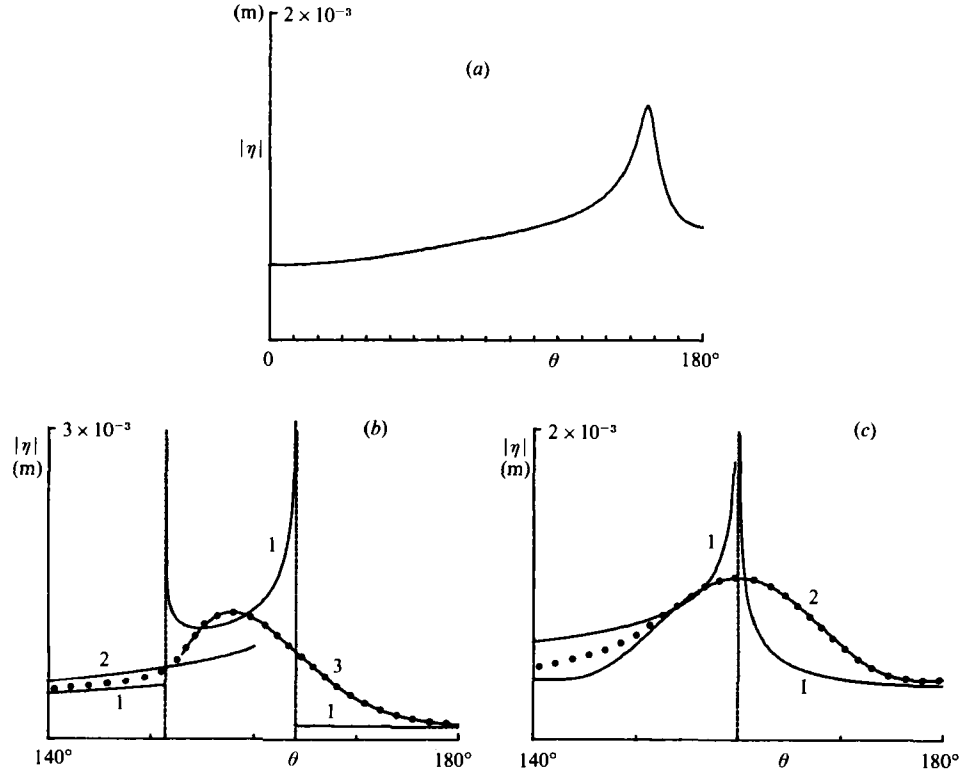

FIGURE 10. Graphs of wave amplitude $|\eta|$ against direction from the source θ, at a distance $r = 1000$ m from the source. The source strength is 5×10^4 kg weight – equivalent to a Hercules C130 aircraft. (*a*) $V = 30$ m/s, there are no caustics, and (3.6) is used throughout. (*b*) $V = 50$ m/s, and there are two caustics, indicated by the vertical dashed lines. (1) is a graph of (3.6); (2) is a graph of (4.1) applied to the caustic at $\theta = 152°$; and (3) is a graph of (4.1) applied to the caustic at $\theta = 164°$. The curve indicated by the large dots represents a reasonable interpolation between the three formulae. (*c*) $V = 37.5$ m/s, and the two caustics have just merged together. (1) is a graph of (3.6), and (2) is a graph of (4.2).

where d is normal distance from the caustic line L in the (x, y)-plane, Ai is the Airy function, and κ_s is $\mathrm{d}\kappa/\mathrm{d}s$ evaluated at P_0, s being arclength along C_k.

Where two points of inflection merge together, both κ and $\mathrm{d}\kappa/\mathrm{d}s$ vanish, and (4.1) predicts infinite amplitudes. At such a point the normal direction could be called a 'supercaustic', and the modified asymptotic expansion for η in the neighbourhood of a supercaustic is derived in the Appendix. We find

$$\eta = \mathrm{i}\frac{\hat{F}(l_0, m_0)}{(\partial B/\partial n)_0} \mathrm{e}^{-\mathrm{i}(l_0 x + m_0 y)} \left[\frac{6}{r\kappa_{ss}}\right]^{\frac{1}{3}} \mathrm{Sc}\left[d\left(\frac{6}{r\kappa_{ss}}\right)^{\frac{1}{3}}\right], \tag{4.2}$$

where the function Sc is analogous to the Airy function in (4.1), and κ_{ss} is $\mathrm{d}^2\kappa/\mathrm{d}s^2$ evaluated at P_0.

Figure 10 shows graphs of wave amplitude against θ. When no caustics are present (3.6) can be used throughout, in which case the r-dependence factors out, so the amplitude-versus-θ graphs are similar for all r, but scaled by the factor $r^{-\frac{1}{2}}$. When caustics are present the amplitude decays with r in two different ways – either as $r^{-\frac{1}{2}}$ normally, or as $r^{-\frac{1}{3}}$ near a caustic – so that a particular value of r must be chosen for the graph. Figure 10(*b*) shows three separate curves, which correspond to (3.6) and

(4.1) applied to each caustic. The best approximation to the amplitude would involve some smooth transition between the curves, as indicated on the figure. For larger r the amplitude graph would be similar to figure 10(b), except that amplitude intensification close to the caustics would be greater because of the $r^{-\frac{1}{3}}$ decay in this region. Figure 10(c) shows the supercaustic case, when (4.2) must be used. All the graphs in figure 10 correspond to a point load, when f is a delta function and $\hat{F}$ a constant.

5. Comparison with measurements

In the Southern Summer of 1982, one of us (J.W.D) made further measurements of ice deflections due to aircraft landing on the runway at McMurdo Sound, using a geophysical wire strainmeter described in detail by Funnell (1982) and shown diagrammatically in figure 11. Since no reference level is available for measuring η directly, waves are detected by measuring changes in curvature of the ice sheet, which cause small changes in the length of a stretched wire. These length changes can be related to the wave amplitude as follows.

The unit normal vector to the ice sheet is given by

$$\hat{\boldsymbol{n}} = \hat{\boldsymbol{z}} - \boldsymbol{\nabla}\eta, \tag{5.1}$$

assuming that $\boldsymbol{\nabla}\eta$ is small. From figure 11 it can be seen that the vector change in wire length due to the wave is

$$\boldsymbol{b}_1, \text{ say, } = \overrightarrow{BB'} - \overrightarrow{AA'} = h_0(\boldsymbol{b}\cdot\boldsymbol{\nabla})\hat{\boldsymbol{n}} \tag{5.2}$$

assuming that b is much less than one wavelength. Taking η proportional to $\exp(\mathrm{i}\boldsymbol{k}\cdot\boldsymbol{x})$, where $\boldsymbol{k} = (l, m)$ is the wavenumber vector, we combine (5.1) and (5.2) to get

$$\boldsymbol{b}_1 = h_0(\boldsymbol{b}\cdot\boldsymbol{k})\,\boldsymbol{k}\eta.$$

The theoretical change in wire length is therefore given approximately by

$$\Delta b = \frac{h_0}{b}(\boldsymbol{b}\cdot\boldsymbol{k})^2\eta. \tag{5.3}$$

The strainmeter is most sensitive to waves whose crests are perpendicular to the wire, when $\boldsymbol{b}\cdot\boldsymbol{k} = bk$. Waves with crests exactly parallel to the wire fail to register, because the posts remain parallel as the wave passes.

By combining (5.3) with (3.6), (4.1) or (4.2) as appropriate, it is possible to predict the response of a strainmeter to the load on the ice during the approach of a landing aircraft, assuming that this load is constant and steadily moving. Actually the air-pressure distribution on the ice does vary in time; since the horizontal dimension of the excess-pressure region under the aircraft is of the order of the aircraft height, the load becomes more concentrated as the aircraft descends. But in any case, as shown in §6, we can approximate the load by a constant point force, or delta-function distribution $f(x, y, t) = W\delta(x - Vt)\,\delta(y)$ with Fourier transform $\hat{F} = W/2\pi$, where W denotes the aircraft weight. Indeed, this approximation will also be valid after the aircraft has touched down. The speed of the aircraft relative to the ground is affected in practice by wind shear and braking on the runway, but the constant-V assumption should be approximately correct, at least during the approach.

To plot a graph of strainmeter response against time, we can regard the strainmeter as moving through the steady wavefield with constant velocity $-V\hat{\boldsymbol{x}}$, along a line

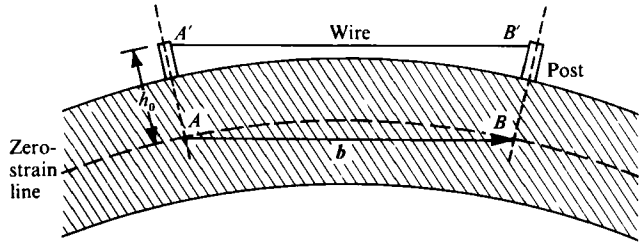

FIGURE 11. Diagram of strainmeter.

y = constant. Figure 12(a) shows a graph of η against time, while 12 (b) and (c) give the response of strainmeters aligned parallel and perpendicular to the runway at the same site. The parallel alignment is responsive to the fast elastic waves propagated in front of the source, since these crests are approximately perpendicular to the runway, while the perpendicular alignment is most sensitive to waves in the transition region (from elastic to gravity waves) where the angle between $\boldsymbol{k}$ and the runway is greatest and $c = c_{\min}$. The predicted response agrees qualitatively with the experimental records shown in figure 13, but the theoretical amplitudes are an order of magnitude larger. This discrepancy can be accounted for by increasing the assumed value of D by a factor of 10. The resulting predicted response is shown in figures 12(d–f). Not only do the amplitudes then agree well, but the rather longer wave periods seem to match the experimental periods more closely.

Additional field work is warranted, however, because of the following experimental uncertainties.

(i) the value of Young's modulus E was not determined independently, and typical quoted values vary from 5×10^8 to 5×10^{10} N/m^2; ice thickness should also be closely monitored;

(ii) it proved difficult to calibrate the strainmeter in the field, so the experimental amplitudes are somewhat uncertain;

(iii) the response of the strainmeter depends on frequency, with a cutoff for frequencies > 1 Hz – which unfortunately falls in the frequency spectrum of the elastic waves;

(iv) the aircraft speed was only roughly estimated – viz, as the airspeed given by the pilot;

(v) the reference point on the recording chart, corresponding to the aircraft position being directly opposite the observer, was not determined.

6. Discussion

The mathematical model adopted should predict the wave system generated by an aircraft landing reasonably accurately, and our results do seem to agree qualitatively with measurements. The wavecrest pattern and wave amplitudes far from the source can be found by simple algebraic methods based on analysis of the wavenumber curve C_k. Numerical analysis is necessary only in finding the caustic angles, since $\kappa = 0$ gives a high-degree algebraic equation which cannot be solved analytically.

Figure 12 shows that the strainmeter deflections arc sensitive to the value of D (which depends linearly on E and on the cube of h), and this parameter could be estimated by comparing theoretical and experimental amplitudes. One possible obstacle may be viscoelastic damping of the waves, which could be of order 10 % over

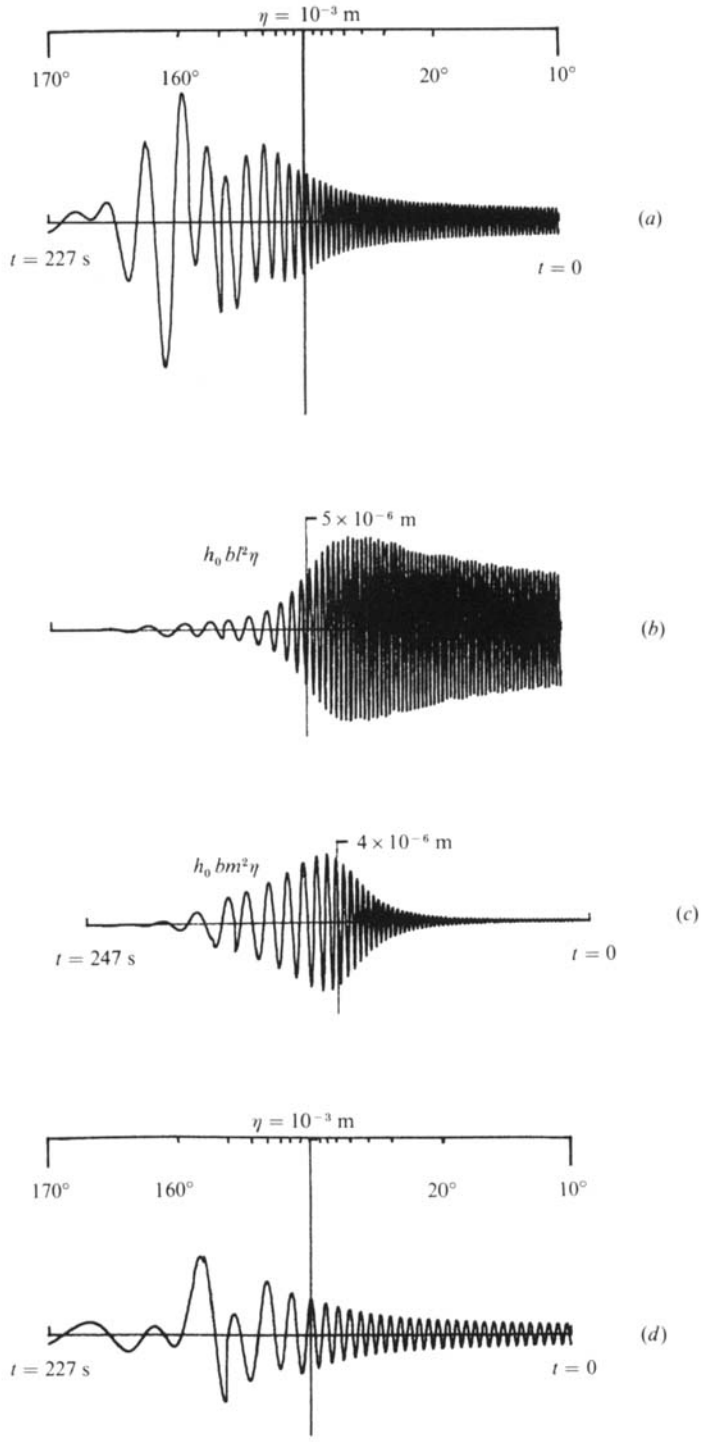

FIGURE 12(*a*, *b*, *c*, *d*). For caption see facing page.

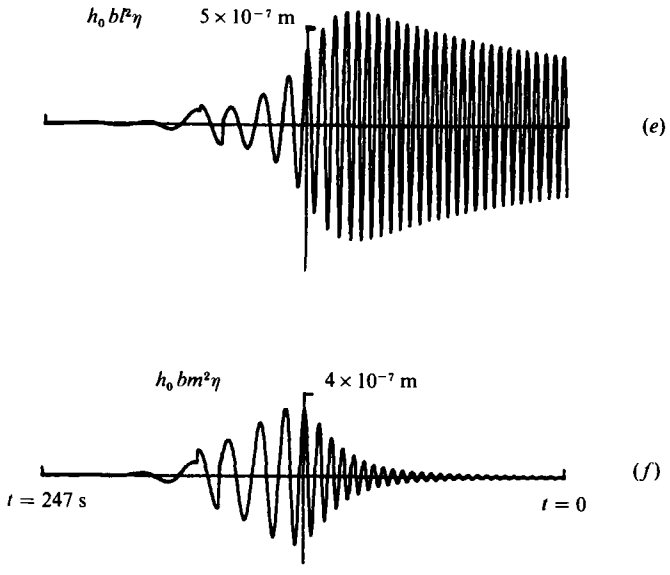

FIGURE 12 (a, b, c). Graphs of theoretical ice displacement and strainmeter response against time t, at a point whose perpendicular distance from the runway is 1000 m, during the approach and landing of a Hercules C130 aircraft of mass 5×10^4 kg. The time interval corresponds to θ (direction of observation point from the aircraft) varying from 10° to 170°. (a) ice displacement; (b) response of a strainmeter parallel to runway; (c) response of a strainmeter perpendicular to runway. For the purposes of comparison with experimental records, the aircraft speed in (a) and (b) is 50 m/s and in (c) is 46 m/s. (d, e, f) These curves correspond to (a, b, c), but the ice rigidity parameter D has been increased by a factor of 10.

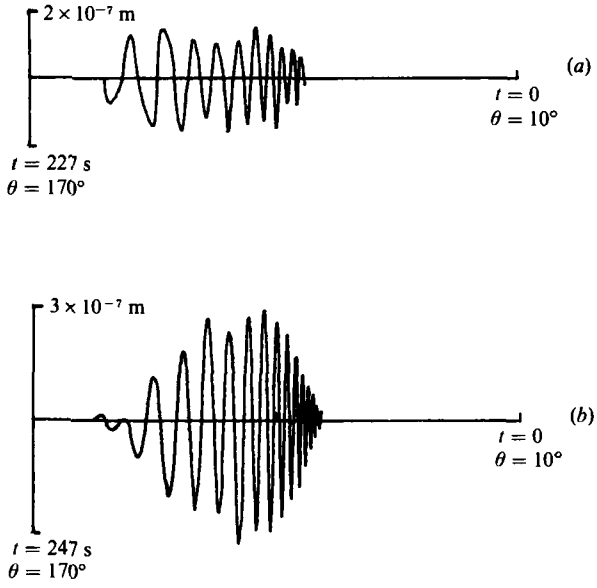

FIGURE 13. Graphs of experimental strainmeter response corresponding to figures 12 (b, e) and 12 (c, f).

a distance of 1 km (Squire & Allan 1980; Bates & Shapiro 1981). An alternative strategy could be to use the phase and period of the oscillations recorded by the strainmeter – which also depend on D – to estimate this parameter; then comparison of the theoretical and experimental amplitudes would also give the viscoelastic damping coefficients. (If phases are to be used it is essential to locate the reference point on the strainmeter record where the aircraft is directly opposite the recording site: $\theta = 90°$.) Thus by careful analysis it should be possible to find detailed information on the ice sheet from the strainmeter record.

The point-source approximation to the aircraft loading function, which has been used throughout, requires some *a posteriori* justification. Effectively we have replaced $\hat{F}(l_0, m_0)$ by the constant $W/2\pi = \hat{F}(0, 0)$ in (3.6), which will be justified if $\hat{F}$ is approximately constant over the range of wavenumbers lying on C_k. As discussed in §5, the lengthscale L for the loading function $f(x, y)$ can be taken to be the aircraft height, or, when the aircraft is close to the ground, its wingspan (≈ 20 m). The Fourier transform $\hat{F}$ will vary significantly over a wavenumber scale $2\pi/L$, so the condition for validity of the point-source approximation is

$$\frac{2\pi}{L} \gg k_0 = (l_0^2 + m_0^2)^{\frac{1}{2}}$$

for all wavenumbers $\boldsymbol{k}_0$ on C_k. This condition can be expressed in terms of wavelengths,

$$L \ll \lambda_0, \tag{6.1}$$

for all wavelengths λ_0 appearing in the steady wave field. For an aircraft travelling at 50 m/s, λ_0 varies from a minimum of 84 m to about 600 m in the vicinity of the caustics, so for an aircraft height of, say, 50 m (6.1) will be satisfied by all but the shortest elastic waves. Calculations have been performed for a reasonably realistic loading function, and the results differ only slightly from those obtained using the point-load approximation (see Davys 1984). This situation is quite different from the ship-wave problem, where the *longest* wavelength is $2\pi V^2/g$ and the wavelength at the caustics where the amplitude is usually greatest is $4\pi V^2/3g$. For a ship travelling at 10 m/s the two figures would be about 60 and 40 m respectively, and are comparable to a typical ship dimension.

The assumptions of a homogeneous ice sheet and uniform water-depth are essential for our analytic methods, but the results should not be sensitive to small-scale inhomogeneities that do not accumulate over a horizontal distance comparable to a characteristic wavelength. We have not considered the effects of lateral stress on the ice sheet (cf. Kerr 1983; Bates & Shapiro 1980), stratification under the ice, nor sea currents, which would introduce anisotropy into the dispersion relation.

Appendix

Expression for η near a supercaustic

Our aim is to find an expression for η far away from the origin and close to a supercaustic line L. To this effect it is convenient to choose axes with L as the x-axis, so η is given by (3.4) in which x is large and y small. Contour integration in the (l, m)-plane (see Lighthill 1978, §4.9) shows that

$$\eta = \mathrm{i} \int_{C_k} \frac{\hat{F}(l, m)}{\partial B/\partial l} \mathrm{e}^{-\mathrm{i}(lx+my)} \, \mathrm{d}m + O(\mathrm{e}^{-\delta_1 x}), \tag{A 1}$$

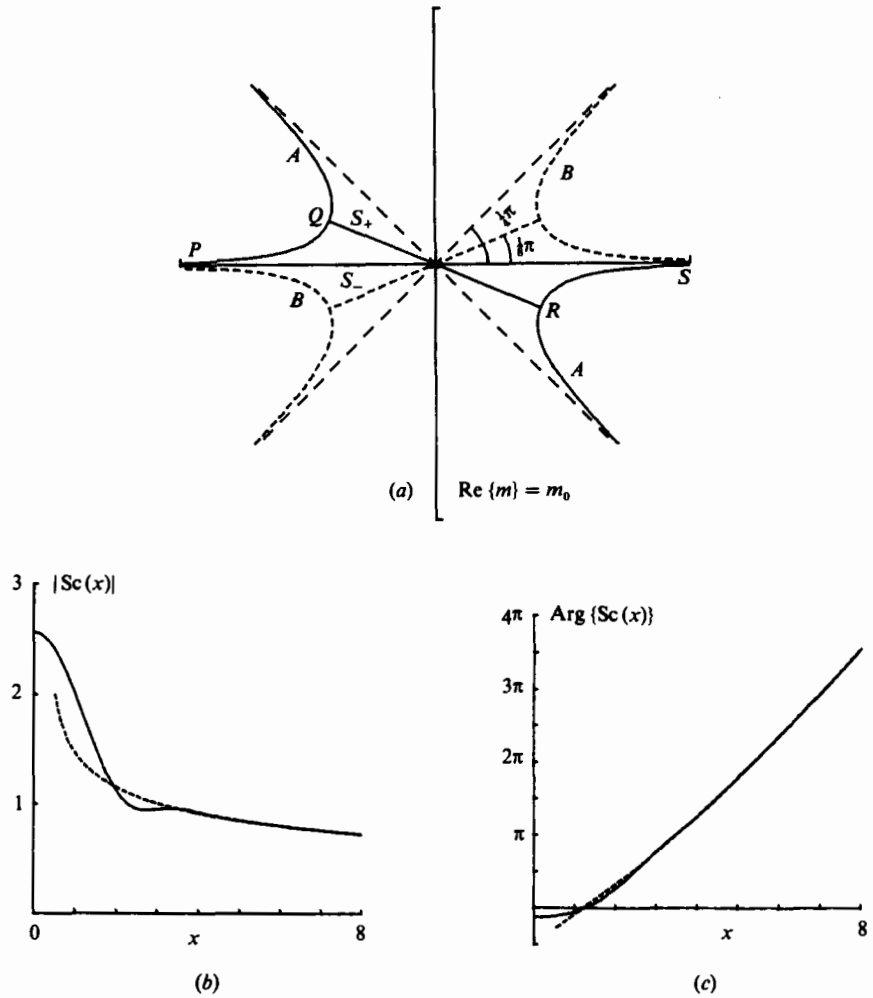

FIGURE 14. (*a*) Contours $\mathrm{Im}\,(l) = -\delta_2$ in the complex m-plane: (A) when $l_0^{(4)} > 0$, and (B) when $l_0^{(4)} < 0$. The contour $PQRS$ represents the integration path when $l_0^{(4)} > 0$. (*b*, *c*) Graphs of the absolute value and argument of $\mathrm{Sc}\,(x)$ against x. The dashed curves show the asymptotic formula (A 5). Note that Sc is an even function, so the graph is drawn only for $x \geqslant 0$.

where δ_1 is some positive constant and C_k the wavenumber curve $B(l, m) = 0$. The contour of integration – i.e. the m-axis – is deformed to paths on which $\mathrm{Im}\,\{l\} = -\delta_2$ (some small positive constant), so that for large x the contribution from integration along such paths is exponentially small. To complete the contour of integration the two disjoint sections of $\mathrm{Im}\,\{l\} = -\delta_2$ must be joined by a path of steepest descent – a straight-line segment passing through the point m_0 where $\mathrm{d}l/\mathrm{d}m = 0$. Since L is a supercaustic, $\mathrm{d}^2l/\mathrm{d}m^2$ and $\mathrm{d}^3l/\mathrm{d}m^3$ also vanish at $m = m_0$, so the integration path close to m_0 is as shown in figure 14(*a*). The only important contribution to η arises from integration along the straight-line segments S_+ or S_-, so that when (to fix our ideas) $(\mathrm{d}^4l/\mathrm{d}m^4)_{m=m_0} = l_0^{(4)}$, say, is positive, we approximate (A 1) by:

$$\eta = \mathrm{i}\frac{\hat{F}(l_0, m_0)}{(\partial B/\partial l)_0}\,\mathrm{e}^{-\mathrm{i}(l_0 x + m_0 y)} \int_{-\infty\,\mathrm{e}^{-\mathrm{i}\pi/8}}^{\infty\,\mathrm{e}^{-\mathrm{i}\pi/8}} \exp\left[-\mathrm{i}\left(\frac{x}{24}\,l_0^{(4)}\,s^4 + O(s^5) + sy\right)\right]\mathrm{d}s, \quad \text{(A 2)}$$

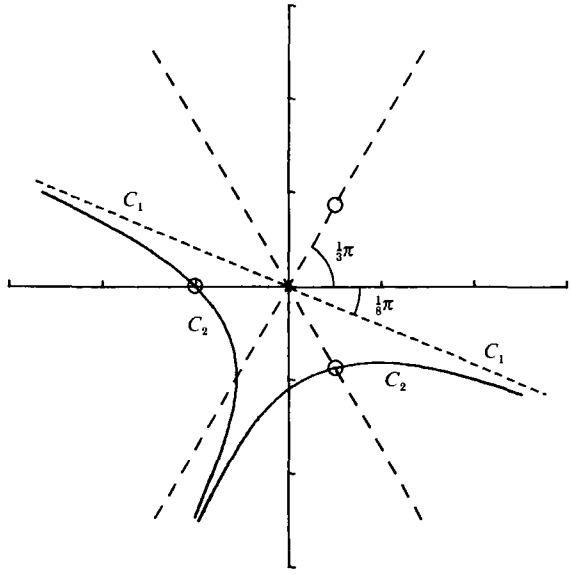

FIGURE 15. Deformation of integration contour C_1 to path of steepest descent C_2. The saddle points $z = -1$, $z = e^{\pm\frac{1}{3}i\pi}$ are circled.

where the integration has been extended to infinity in both directions without introduction of further significant error, since the integrand is exponentially small. Writing (A 2) in a form that is independent of the choice of (x, y)-axes and making the substitution

$$s = \left(\frac{6}{xl_0^{(4)}}\right)^{\frac{1}{4}}\xi,$$

we finally obtain

$$\eta = i\frac{\hat{F}(l_0, m_0)}{(\partial B/\partial n)_0} e^{-i(l_0 x + m_0 y)} \left[\frac{6}{r\kappa_{ss}}\right]^{\frac{1}{4}} \mathrm{Sc}\left[d\left(\frac{6}{r\kappa_{ss}}\right)^{\frac{1}{4}}\right], \tag{A 3}$$

where $\kappa_{ss} = d^2\kappa/ds^2$ at the point (l_0, m_0) on C_k from which the supercaustic emanates, d is perpendicular distance from L, and the 'supercaustic function' Sc is defined by

$$\mathrm{Sc}(x) = \int_{-\infty e^{-i\pi/8}}^{\infty e^{-i\pi/8}} e^{-i(\xi x + \frac{1}{4}\xi^4)}\, d\xi. \tag{A 4}$$

If $d^2\kappa/ds^2$ is negative then the necessary modifications to (A 3) are that κ_{ss} mean $|d^2\kappa/ds^2|$ and that the function Sc be replaced by its complex conjugate. Figures 14(b, c) show numerically calculated graphs of the absolute value and argument of Sc.

Asymptotic form of Sc(x)

An asymptotic expansion of Sc(x) for large x can be found using the method of steepest descent. We transform the integral in (A 4) by setting $\xi = x^{\frac{1}{3}}z$ and obtain

$$\mathrm{Sc}(x) = x^{\frac{1}{3}} \int_{-\infty e^{-i\pi/8}}^{\infty e^{-i\pi/8}} e^{x^{4/3}h(z)}\, dz,$$

where $h(z) = -i[z + \frac{1}{4}z^4]$. The zeros of $h'(z)$, or saddle points, occur at $z = e^{\pm\frac{1}{3}i\pi}$ and $z = -1$; and using the methods described by Ursell (1970), the contour of integration

can be deformed into a path of steepest descent passing through $z = -1$ and $z = e^{-\frac{1}{3}i\pi}$ (figure 15). Since the real part of $h(z)$ is greater at $z = -1$ the contribution from this saddle point is dominant and Watson's lemma can be used in the standard way to give

$$\mathrm{Sc}(x) \approx \pi^{\frac{1}{2}} \exp\left(\tfrac{3}{4}ix^{\frac{4}{3}}\right)\left[\frac{1}{\sqrt{3}}(1-i)\,x^{-\frac{1}{3}} - \frac{7\sqrt{3}(1+i)}{108}x^{-\frac{5}{3}} + \ldots\right]. \tag{A 5}$$

The asymptotic formula is also graphed in figure 14.

R. B. Paris has drawn our attention to the fact that $\mathrm{Sc}(x)$ can be expressed in terms of special functions considered by Bakhoom (1933), and that the asymptotic formula (A 5) can be derived using results given in that paper.

We wish to thank Professor B. S. Liley and Mr R. Holdsworth, of the Physics Department of the University of Waikato, for essential help with the experimental work. We are also indebted to a referee for suggesting the approximation (2.6) to the dispersion relation.

REFERENCES

Bakhoom, N. G. 1933 Asymptotic expansions of the function $F_k(x) = \int_0^\infty e^{u^k + xu}\,du$. *Proc. Lond. Math. Soc.* (2) **35**, 83.

Bates, H. F. & Shapiro, L. H. 1980 Long-period gravity waves in ice-covered sea. *J. Geophys. Res.* **85** (C2), 1095.

Bates, H. F. & Shapiro, L. H. 1981 Stress amplification under a moving load on floating ice. *J. Geophys. Res.* **86** (C7), 6638.

Davys, J. W. 1984 Waves in floating ice plates. M.Sc. thesis, University of Waikato.

Funnell, R. H. 1982 Waves in sea ice. M.Sc. thesis, University of Waikato.

Greenhill, A. G. 1887 Wave motion in hydrodynamics. *Am. J. Maths* **9**, 62.

Kerr, A. D. 1976 The bearing capacity of floating ice plates subjected to static or quasistatic loads. *J. Glaciol.* **17**, 229.

Kerr, A. D. 1983 The critical velocities of a load moving on a floating ice plate that is subjected to inplane forces. *Cold Regions Sci. Tech.* **6**, 267.

Kheisin, D. Ye. 1971 Some non-stationary problems of dynamics of the ice cover. In *Studies in Ice Physics and Ice Engineering* (ed. Iakolev). Israel Program for Scientific translations.

Lighthill, M. J. 1978 *Waves in Fluids*. Cambridge University Press.

Longuet-Higgins, M. S. 1977 Some effects of finite steepness on the generation of waves by wind. In *A Voyage of Discovery: George Deacon 70th Anniversary Volume* (ed. M. Angel). Pergamon.

Mills, D. A. 1972 Waves in a sea ice cover. *Horace Lamb Centre for Oceanog. Res., Flinders Univ. S. Australia, Res. Rep.* 53.

Nevel, D. E. 1970 Moving loads on a floating ice sheet. *US Army CRREL Res. Rep.* 261.

Squire, V. A. & Allan, A. J. 1980 Propagation of flexural gravity waves in sea ice. In *Sea Ice Processes and Models* (ed. R. S. Pritchard). University of Washington Press.

Squire, V. A., Robinson, W. H., Haskell, T. G. & Moore, S. C. 1985 Dynamic strain response of lake and sea ice to moving loads. *Cold Regions Sci. Tech.* (to appear).

Ursell, F. 1970 Integrals with a large parameter. Paths of descent and conformal mappings. *Proc. Camb. Phil. Soc.* **67**, 371.